Real-time reconstruction of three-dimensional cylindrical near-field radar images using a single instruction multiple data interpolation approach

D. Flores-Tapia[1]   C.M. Alabaster[2]   S. Pistorius[3,*]

[1]Department of Mathematics, University of Manitoba, Division of Medical Physics, CancerCare Manitoba, Winnipeg, Manitoba, Canada R3E 0V9
[2]Department of Informatics and Systems Engineering, Cranfiled University, Shrivenham SN6 8LA, UK
[3]Department of Research, CancerCare Manitoba, Winnipeg, Manitoba, Canada R3E 0V9
*Departments of Physics and Astronomy and Radiology, University of Manitoba, Winnipeg, Manitoba, Canada R3T 2N2
E-mail: daniel.florestapia@cancercare.mb.ca

Abstract: During the last decade, radar imaging has been used in near-field scenarios where a cylindrical scan geometry is required to properly illuminate the scan region, such as breast microwave radar imaging and microwave wood inspection. Nevertheless, current cylindrical near-field radar image formation algorithms are not fast enough to provide the throughput required by these novel applications. A real-time wavefront reconstruction approach for the formation of three-dimensional cylindrical near-field radar images is proposed in this study. This technique parallelises the mapping procedures during the reconstruction process in order to increase its computational efficiency. To further reduce the execution time of the proposed approach, it was implemented in a general purpose graphic processing unit in order to take advantage of the computing capabilities of this platform. The proposed method yielded accurate results when applied to simulated and experimental data sets and yielded speed improvements of two orders of magnitude compared to conventional cylindrical near-field radar reconstruction approaches.

1 Introduction and motivation

During the last three decades, cylindrical radar imaging has proven to be a reliable tool for imaging and sensing a number of scenarios [1–4]. The basis of this imaging technology is the dielectric differences between the materials that form the scan region propagation medium and the targets present inside it [1]. In recent years, cylindrical scan trajectories have been used in some novel near-field radar applications, such as microwave wood inspection (MWI) and breast microwave radar imaging (BMRI), because this geometry better suits the shape of the scan regions in these situations [5, 6]. As the irradiation is performed along the scan trajectory, the target responses have different travel times, resulting in the formation of non-linear signatures [7]. This makes it difficult to correctly determine the dimensions and locations of the different scattering structures present in the scan area. In order to properly visualise the targets reflections, the collected data must be focused [5–8].

A number of techniques have been proposed to reconstruct cylindrical near-field radar images. In general, these methods can be classified as either time-shift techniques or wavefront reconstruction approaches. Time-shift techniques perform a shift-sum process over a set of regions of interest in the scan area. Two examples of this approach are the confocal mapping algorithm [5, 9] and the beamforming reconstruction

method [8]. Wavefront reconstruction approaches focus the data by processing the spectrum of the collected responses and transforming it from the spatial-temporal domain where it is originally acquired to the spatial domain where it will be displayed [7]. Although each method has advantages and disadvantages of their own, time-shift techniques are simpler to implement and debug, whereas wavefront reconstruction approaches exhibit a higher signal-to-noise ratio (SNR) and an increased focal quality [7].

A problem with cylindrical radar reconstruction approaches is their execution time. Its computational complexity is of the order of $O(\bar{n} \log \bar{n})$, where $\bar{n}$ is the input signal length, resulting in execution times of the order of minutes per scan plane when executed in a conventional multicore Pentium CPU [10]. This can be an issue in the scenarios such as the ones in which cylindrical near-field radar is used, owing to the fact that a low execution time is required to provide the high throughput that is needed [11]. In this paper, the use of a single instruction multiple data (SIMD) architecture is proposed to form real-time three-dimensional (3D) radar images recorded in cylindrical near-field scenarios using a wavefront reconstruction approach. In the scope of this paper, an approach is considered to be real-time if its reconstruction time is less than the data acquisition time of a range profile, which is around 5 s. This follows the standard definition, where a system or

approach is considered to be real-time if it is able to update information at the same rate as it receives data. The work presented in this paper expands the work presented by the authors in [12] into three fundamental areas. First, it formulates a generalisation into a 3D scan geometry. Second, the approach is expanded to a generic SIMD computing architecture to allow the use of multiple computing devices. Third, the performance of the proposed method is evaluated using experimental datasets in order to assess its feasibility in realistic scenarios.

The proposed approach uses a novel interpolation approach that is executed in parallel, significantly reducing the reconstruction time without compromising the spatial accuracy and SNRs of the resulting images. Since each point in the problem space can be processed independently, the proposed technique was implemented using an approach on a general purpose graphics processing unit (GPGPU) to take advantage of the high-performance computing capabilities of this platform. Originally used for computer graphic applications, GPGPU devices are being increasingly used for scientific applications, ranging from protein folding to the finite-element analysis, because of their low cost, high memory bandwidth and enormous arithmetic capabilities [13–17]. The performance of the proposed method was evaluated using a set of simulated and experimental data sets. The execution time, SNR and spatial accuracy of the reconstructed images were calculated in order to assess the performance of the proposed technique.

2 Cylindrical SR imaging

2.1 Signal model

Let us consider a cylindrical scan geometry with M scan planes defined along the z-axis and N scan locations arranged in a circular pattern with a radius R at each plane. The irradiating antenna is facing towards the centre of the scan plane. T point scatters are assumed to be inside the area delimited by the scan geometry. A waveform $f(t)$ with a bandwidth B, is sequentially radiated from each scan location and the responses from the targets with the scan area are recorded at the same position. This signal is considered to have a length of L samples. For the scan location at (R, θ, z), the received signal can be expressed as

$$s(t, \theta, z) = \sum_{q=1}^{T} \sigma_q f\left(t - \frac{2D_q(\theta, z)}{\nu}\right) \quad (1)$$

where ν is the medium propagation speed, σ_q and (r_p, ϕ_q, z_p) are the reflectivity and location of the qth target, and $D_q(\theta, z) = \sqrt{R^2 + r_q^2 + (z_q - z)^2 - 2Rr_q \cos(\phi_q - \theta)}$.

In cylindrical SR scenarios, target reflections present non-linear signatures because of the different signal travel times along the different scan locations [7] and the near field distances between the targets and the scan geometry. As illustrated in Fig. 1, this makes it difficult to assess the locations and dimensions of the targets present in the scan area. To properly assess the target dimensions and locations, the data must be reconstructed. An effective way of doing this is by using wavefront reconstruction methodology [18, 19]. The first step is to calculate the Fourier transform of (1) along the t, z and θ directions and compensate for the phase and magnitude effects of the scan geometry. By using the mathematical procedure described in [7] to compensate for
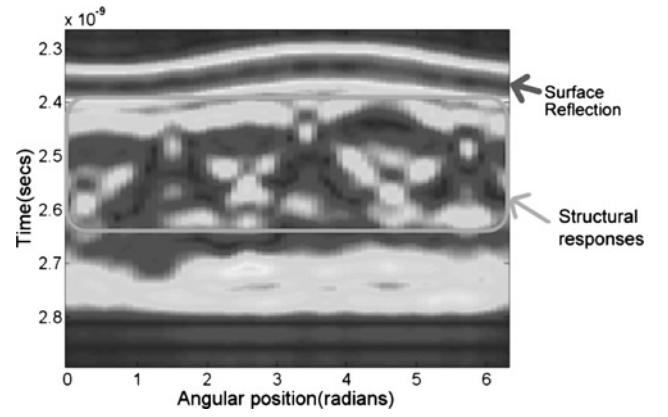
Fig. 1 *Unprocessed 2D image from an experimental data set containing a single target*

the compensated dataset, $U(\omega, \varepsilon, k_z)$, is given by

$$U(\omega, \varepsilon, k_z) = \sum_{q=1}^{T} 4\sigma_q \cdot \xi(\omega, \varepsilon, k_z)$$

$$\times \exp\left(\begin{array}{c} -j\left(\sqrt{(4k^2 - k_z^2)r_q^2 - \varepsilon^2}\right) \\ + \varepsilon \cdot \sin^{-1}\left(\varepsilon / \sqrt{(4k^2 - k_z^2)r_q^2}\right) + \varepsilon\phi_q + k_z z_q \end{array}\right)$$

$$(2)$$

where ε and k_z are the spatial frequency counterparts of θ of z, respectively, k is the wavenumber, $\omega = 2\pi f$, and $\xi(\omega, \varepsilon, k_z)$ is the spectrum amplitude component in the $(\omega, \varepsilon, k_z)$ frequency space.

The next step is to transfer the data from $U_p(\omega, \varepsilon, k_z)$ to the (k_x, k_y, k_z) spatial frequency space, where k_x and k_y are the spatial frequency counterparts of x and y spatial domains. First, a magnitude filter given by $\sqrt{\varepsilon^2 / \sqrt{(4k^2 - k_z^2)R^2 - \varepsilon^2}}$ is applied to correct for the variable density of the polar grid. This filter was derived using the stationary phase [18] principle and it is used to assure a one to one correspondence between the responses in the Cartesian and polar frequency spaces. Next, the inverse Fourier transform of (2) is along ε is calculated, yielding a function denoted as $S_c(\omega, \theta, k_z)$, and the following mapping functions are used [7]

$$k_{ur} = \sqrt{4k^2 - k_z^2} \quad (3)$$

$$k_{ux} = k_{ur} \cdot \cos(\theta) \quad (4)$$

$$k_{uy} = k_{ur} \cdot \sin(\theta) \quad (5)$$

These mappings produce an unevenly sampled frequency space, denoted as $I(k_{ux}, k_{uy}, k_z)$, because the separation between adjacent samples in k, k_z and θ is constant. Nevertheless, conventional FFT techniques present limitations when it comes to process this kind of frequency space [18]. In order to process the compensated data using standard Fourier methods, the evenly sampled frequency space, (k_x, k_y, k_z), is defined as follows

$$k_x = k_y = n\pi/R \text{ for } -N \leq n \leq N \quad \text{and} \quad n \in \mathbb{Z} \quad (6)$$

$$k_z = m \cdot 2\pi/(M \cdot \Delta z) \text{ for } 0 \leq m \leq eM - 1 \text{ and } m \in \mathbb{Z} \quad (7)$$

where dz is the distance between adjacent scan planes. Next, the evenly sampled spectrum $I(k_x, k_y, k_z)$ is obtained by interpolating the values of $I(k_{ux}, k_{uy}, k_{uz})$ at the points defined in (k_x, k_y, k_z). Finally, the 3D inverse Fourier transform of $I(k_x, k_y, k_z)$ is calculated, yielding the 3D model $i(x, y, z)$. A more detailed explanation of the 3D cylindrical holographic reconstruction technique is given in [7].

2.2 Interpolation of unevenly sampled spaces

The most computationally intensive portion of the 3D wavefront reconstruction approach is the interpolation process. In non-evenly sampled frequency spaces, the interpolation procedure is performed using a series of triangulation operations in which the values of (k_{ux}, k_{uy}) and (k_{ur}, k_z) spaces are used to determine the basis that will be used to calculate each element in (k_x, k_y, k_z). This approach is also known as Qhull interpolation [19].

The Qhull method can be described as follows. Consider the two-dimensional (2D) case that leads to the formation of each (k_x, k_y) plane, where we define a set $\{P_1, P_2, P_3, \ldots, P_i, \ldots, P_\gamma\}$. P_i is the ith-ordered pair in each (k_{ux}, k_{uy}) plane and $\gamma = L \cdot N$. A triangulation φ is a set of A triples of points (P_a, P_b, P_c), where $a, b, c \in \{1, 2, 3, \ldots, \gamma\}$ and (P_a, P_b, P_c) are pairwise distinct such that for each triple, the corresponding points are the vertices of a triangle with the properties that each such triangle contains only those three points of P and those are the vertices, that the intersection of the interiors of any two triangles is empty, and that the unions of those triangles is the complex hull of P [19, 20]. For any set of points, there are almost always several triangulations. To optimise this topological process, a Delaunay triangulation algorithm is often used. This approach optimises the triangulation process by evaluating the smallest angle in each of the possible triangulations present in the evaluated set [20]. This algorithm is described in detail in [20]. After this step, various interpolation bases can be used to generate a function $I(k_x, k_y, k_z)$ that describes the behaviour of the data contained in (k_{ux}, k_{uy}) over the frequency values defined in (k_x, k_y). A 3D generalisation of this approach is used to generate $I(k_x, k_y, k_z)$ the from $U(\omega, \varepsilon, k_z)$.

Another possible approach to generate evenly sampled spectra from unevenly sampled spaces is by using the inverse non-uniform inverse FFT(NFFT^H). This technique performs a convolution process using a predefined kernel in the frequency domain to generate the equidistant samples from a set of non-evenly sampled locations. After this estimation is performed, the inverse fast Fourier transform (FFT) of the evenly sampled dataset is calculated. Finally, a deapodisation step is performed using the time-domain representation of the kernel in order to eliminate its effect. NFFT^H approaches have been widely used for a wide variety of reconstruction problems, ranging from magnetic resonance imaging to ultrasound tomography [21–25]. This technique yields images with a comparable accuracy and focal quality when compared with Qhull approaches when used to form radar images [26].

3 SIMD interpolation

3.1 Description

Qhull approaches have an expected performance of $O(\bar{n} \log \bar{n})$, which in cylindrical SR imaging applications usually results in execution times of 35 s to 1 min per

imaging plane when executed on a standard Pentium multicore CPU [7]. The interpolation procedure is the most computationally intensive portion of the reconstruction process as the rest of the reconstruction takes less than 1% of the execution time. The order of complexity of this operation is on the same order as the FFT, but the additional execution time is caused by the fact that the number of samples in (k_x, k_y, k_z), $(2(L-1)+1)^2 \cdot M$, is generally much higher than the number of elements in the (ω, θ, k_z) space, since in the majority of the radar systems $L \gg N$. On the other hand, NFFT^H approaches also have a complexity of the order of, where is the number of points in the original dataset [21]. Although these approaches can be parallelised to increase the data throughput, they have only been tested on datasets smaller (512×512 samples) than the ones found in radar imaging scenarios and they are only used for 2D resampling in each imaging plane [21]. Further investigation is required to optimise the use of these approaches for 3D cylindrical SR reconstruction.

In order to reduce the execution time of the reconstruction process, an SIMD approach is proposed in this paper. SIMD programming models are used to parallelise computationally expensive procedures in order to reduce its execution time. SIMD approaches can be easily implemented in GPGPU devices, which are quite effective to tackle problems that require a large number of interpolation operations since they use specialised hardware for this purpose. GPGPU devices process several data elements in parallel using different threads running the same program, which we will refer to as a kernel. A full description of the capabilities of GPGPU computing is well beyond the scope of this paper, we will only address the key points of the implementation of the proposed approach on the GPGPU platform. If the reader wants to further investigate about the potential of this computing platform to solve complex Fourier imaging problems, a very detailed description is given in [17, 21, 22].

Current GPGPU interpolation procedures are designed to work only on evenly separated spaces. This fact, in addition to its high number of branching operations, thus makes the implementation of the Qhull approach on a GPGPU platform very difficult. In order to take advantage of the GPU computing capabilities, an interpolation approach that works over an evenly spaced grid must be used. Let consider the a discrete $(2L+1) \times (2L+1) \times M$ frequency space (k_x, k_y, k_z) as defined in (6) and (7). According to the inversion technique described in Section 2, after the effects of the scan geometry are compensated, the collected data must be transferred from the (ω, θ, k_z) to the (k_x, k_y, k_z) space. To migrate the responses from each (k, k_z) plane to their corresponding d (k_r, k_z) space using an interpolation approach that considers an evenly sampled space, we will first define an auxiliary function

$$p(k_r, k_z) = \sqrt{k_r^2 + k_z^2} \qquad (8)$$

$$k_r = l \cdot \pi/(L \cdot dt) \text{ for } 0 \le l \le L - 1 \quad \text{and} \quad l \in \mathbb{Z} \qquad (9)$$

where dt is the sampling period of $f(t)$. At this point, the value of the $U(\omega, \varepsilon, k_z)$ along the evenly sampled points defined by (k_r, k_z) can be calculated by interpolating over the components $U(\omega, \varepsilon, k_z)$ at the points specified in their corresponding $(p(k_r, k_z), k_z)$ values, since data points in (ω, θ, k_z) are evenly sampled, yielding the intermediate spectrum $U(\omega, \theta, k_z)$. Next, the polar coordinates of each

point in (k_x, k_y) can be calculated as follows

$$\psi(k_x, k_y) = \sqrt{k_x^2 + k_y^2} \qquad (10)$$

$$\vartheta(k_x, k_y) = \begin{cases} \tan^{-1}(k_x/k_y), & \text{if } k_x > 0 \text{ and } k_y \geq 0 \\ \tan^{-1}(k_x/k_y) + 2\pi, & \text{if } k_x < 0 \text{ and } k_y \geq 0 \\ \tan^{-1}(k_x/k_y) + \pi, & \text{if } k_x < 0 \text{ and } k_y < 0 \\ \pi/2, & \text{if } k_x = 0 \text{ and } k_y > 0 \\ 3\pi/2, & \text{if } k_x = 0 \text{ and } k_y < 0 \\ 0, & \text{if } k_x = 0 \text{ and } k_y = 0 \end{cases}$$

$$(11)$$

We can now define the auxiliary discrete frequency space (ρ, φ) where ρ and φ are the ranges of $\psi(k_x, k_y)$ and $\vartheta(k_x, k_y)$, respectively. The values of $U(\omega, \theta, k_z)$ at the points contained in (ρ, φ) can be calculated by using a interpolation approach that considers evenly sampled data points. This set of values will be denoted as $S_c(\rho, \varphi)$. Next, we can map $U(\omega, \theta, k_z)$ into the (k_x, k_y, k_z) frequency space using the following function

$$I(\alpha(\rho, \varphi), \beta(\rho, \varphi), k_z) = \bar{U}(\rho, \varphi, k_z) \qquad (12)$$

where

$$\alpha(\rho, \varphi) = \rho \cdot \cos(\varphi) \qquad (13)$$

$$\beta(\rho, \varphi) = \rho \cdot \sin(\varphi) \qquad (14)$$

Since (11) is the inverse of the mapping process described in (5) and (6), and both relations have a one-to-one relation, it is not difficult to prove that the $\alpha(\rho, \varphi)$ and $\beta(\rho, \varphi)$ map the points in (ρ, φ) back into each (k_x, k_y) plane; therefore $I(\alpha(\rho, \varphi), \beta(\rho, \varphi), k_z)$ can be regarded as a single plane in $I(k_x, k_y, k_z)$ and it does not have any gaps within its spectral support band. Finally, the 3D inverse fast Fourier transform (IFFT) of $I(\alpha(\rho, \varphi), \beta(\rho, \varphi), k_z)$ is calculated to properly visualise the reconstructed data in the spatial domain. An illustration of how the proposed interpolation approach is shown in Fig. 2. In this diagram, the location of random

Fig. 2 *Flow diagram of the proposed 3D GPU interpolation algorithm*

samples in the (k_x, k_y) and (k_r, k_z) planes is shown using different colours. Note how their corresponding locations in the (k_r, θ) and (k, k_z) spaces do not fall exactly into a particular cell. The location of the samples that are more likely to calculate their values is denoted using a lighter version of the sample colours.

3.2 Implementation

Each location on the (k_x, k_y, k_z) and (k_r, k_z) frequency spaces is processed using an individual kernel. Owing to the size of the problem domain, the global, constant and texture memory structures of the GPGPU were used. The main reason that a GPGPU platform was chosen as the computing platform for the proposed approach is that the texture memory in this kind of devices is able to perform a significantly fast linear or nearest-neighbour interpolation fitting [27]. In contrast to the other memory modules, compute unified device architecture (CUDA) allows the user to use floating numbers to address the elements residing in the texture memory, also known as textels. When a fetch to a non-integer address is performed, the returned value is the result of the interpolation between the textels closer to the requested address [27]. This property is used by the proposed method to perform the interpolation processes over the (k_x, k_y) and (k_r, k_z) planes.

The execution of the proposed method in a GPU platform can be described step by step as follows:

1. Transfer the values of $S_c(\omega, \theta, k_z)$ from host to the device texture memory, and the values of $\Delta k = 2\pi/(L \cdot dt)$, Δz and R from the device constant memory.
2. The variables $I, k_x, k_y, \rho, \varphi, \psi, k_z, k_r, U$ and p are then defined in the GPU global memory.
3. A kernel is executed over a grid with $L \times M$ threads, $G_{r,z}$ to initialise the values of k_z, k_r and $p(k_r(g_r), k_z(g_z))$ as follows

$$k_r(g_r) = g_r \cdot \Delta k \qquad (15)$$

$$k_z(g_z) = g_z \cdot 2\pi/(M \cdot \Delta z) \qquad (16)$$

$$p(k_r(g_r), k_z(g_z)) = \sqrt{k_r(g_r)^2 + k_z(g_z)^2} \qquad (17)$$

$$\forall(g_r, g_z) \in G_{r,z}$$

where g_r and g_z are the column and row indexes of the gth element of $G_{r,z}$, and

$$g_r = n_r \in \mathbb{Z} \quad \text{and} \quad 0 \leq n_r \leq L - 1 \qquad (18)$$

$$g_z = n_z \in \mathbb{Z} \quad \text{and} \quad 0 \leq n_z \leq M - 1 \qquad (19)$$

This definition of $k_r(g_r)$ and $k_z(g_z)$ is equivalent to the one given in (8) and (10) by making the index substitutions $g_r = l$ and $g_z = m$.
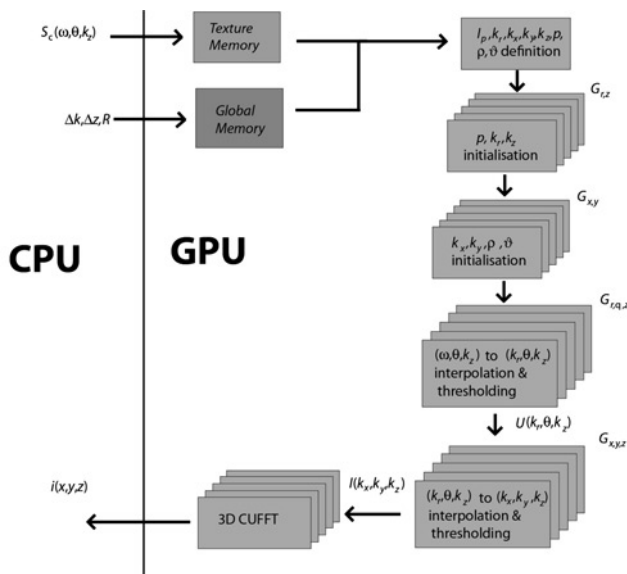4. The locations of each sample in the (k_x, k_y) space are initialised using a kernel that is executed over a grid containing $2(L-1) + 1 \times 2(L-1) + 1$ threads, $G_{x,y}$ This kernel performs the following operations:
(a) Determines the values of k_x and k_y using the following expressions

$$k_x(g_x) = (g_x - N)\pi/R \qquad (20)$$

$$k_y(g_y) = (g_y - N)\pi/R \qquad (21)$$

$$\forall(g_x, g_y) \in G_{x,y}$$

where g_x and g_y are the column and row indexes of the gth element of $G_{x,y}$ and

$$g_x = n_x \in \mathbb{Z} \quad \text{and} \quad 0 \leq n_x \leq 2(L-1) \qquad (22)$$

$$g_y = n_y \in \mathbb{Z} \quad \text{and} \quad 0 \leq n_y \leq 2(L-1) \qquad (23)$$

The previous definition of $k_x(g_y)$ and $k_y(g_y)$ is equivalent to the one given in (6) by making the index substitutions g_x or g_y equal to the n.

(b) Calculates the values of, ρ, φ from the values of $k_x(g_y)$ and $k_y(g_y)$ using (9) and (10)

$$\rho(k_x(g_x), k_y(g_y)) = \psi(k_x(g_x), k_y(g_y)) \quad \text{and}$$

$$\varphi(k_x(g_x), k_y(g_y)) = \vartheta(k_x(g_x), k_y(g_y)) \quad \forall (g_x, g_y) \in G_{x,y} \qquad (24)$$

5. A kernel is executed on a grid containing $L \times M \times N$ threads, $G_{r,\theta,y}$. This kernel performs the two tasks:

(a) Interpolate the values of $U(p(k_r(g_r), k_z(g_z)), \theta(g_\theta), k_z(g_z))$, where $g_\theta = n_\theta \in \mathbb{Z}$ and $0 \leq n_\theta \leq N-1$, by performing a texture memory fetch from $S_c(\omega, \theta, k_z)$ for each (g_r, g_θ) component in $G_{r,\theta,y}$ using their corresponding $p(k_r(g_r), k_z(g_z))$ values as addresses.

(b) Perform a thresholding process to each element as $U(p(k_r(g_r), k_z(g_z)), \theta(g_\theta), k_z(g_z))$ follows (see (25))

where $k_{max} = \Delta k(L-1)$.

6. Interpolate the values in each (k_x, k_y) plane using a kernel on a grid with $2(L-1)+1 \times 2(L-1)+1 \times M$ threads, $G_{x,y,z}$. This kernel performs two operations:

(a) Interpolate the values of $I(k_x(g_x), k_y(g_y), k_z(g_z))$ by performing a texture memory fetches from $U(p(k_r(g_r), k_z(g_z)), \theta(g_\theta), k_z(g_z))$ using the corresponding values $\rho(k_x(g_x), k_y(g_y))$ and $\varphi(k_x(g_x), k_y(g_y))$ of each element in $G_{x,y,z}$.

(b) Apply a thresholding criterion to each element as follows

$$I(k_x(g_x), k_y(g_y), k_z(g_z))$$
$$= \begin{cases} I(k_z(g_x), k_y(g_y), k_z(g_z)) & \text{if } (k_x(g_x), k_y(g_y), k_z(g_z)) \leq 2k_{max} \\ 0 & \text{otherwise} \end{cases} \qquad (26)$$

7. The 3D IFFT of $I(k_x(g_x), k_y(g_y), k_z(g_z))$ is calculated and the result is then transferred to the host memory for further processing.

A flow diagram of this process is displayed in Fig. 3.

4 Simulation and experimental setup

The performance of the proposed method was assessed using both simulated and experimental data sets. The simulated data sets were generated using the radar simulator proposed by the authors in [28]. The accuracy of this simulation technique on high-contrast scenarios has been proved using finite difference time domain simulation techniques. The datasets had four different sizes $127 \times 72 \times 11$, $251 \times 72 \times 11$, $501 \times 150 \times 16$ and $1001 \times 150 \times 16$ points and
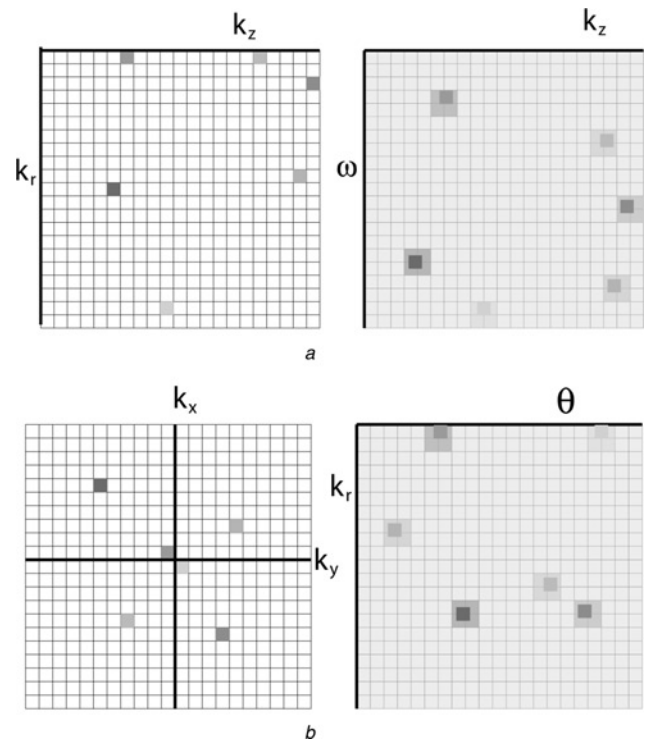

Fig. 3 *Diagram of the mapping process*
a (k_r, k_z) to (ω, k_2)
b (k_x, k_y) to (k_r, θ)

contained white Gaussian noise with a power of -70 dBm. A stepped frequency continuous wave (SFCW) with a bandwidth of 11 GHz (centre frequency of 6.5 GHz) and a power of 0 dBm was used as the radiated waveform. In these simulated data sets, the radius of the scan region was 10 cm for the $127 \times 72 \times 11$ and $251 \times 72 \times 11$ datasets and 15 cm for the rest. The number of targets were randomly assigned between one and five.

The experimental data in the first three experiments were collected using the SFCW Radar system described in [7]. The system consists of a 360B wiltron network analyser and an AEL H horn antenna with a length of 19 cm and a width of 12 cm. This antenna is mounted on a custom automated mechanism in which the phantom is rotated to emulate a cylindrical scan geometry. A SFCW with a bandwidth of 11 GHz (1–12 GHz) was used in the first three experiments. The system was characterised by recording the antenna responses inside an anechoic chamber. This reference signal was subtracted from the experimental data in order to eliminate the distortions introduced by the system components. The data acquisition setup was surrounded by electromagnetic wave absorbing material in order to reduce undesirable environment reflections. To assess the performance of the proposed approach in scenarios where a lower dielectric contrast is present, a fourth experiment was performed using a preclinical breast microwave radar (BMR) data acquisition system. This system was formed by a plexi glass tank of $56 \times 56 \times 40$ cm with a Vivaldi antenna attached to its posterior wall. This tank was filled using canola oil to provide an impedance matching between the antenna and the breast phantom. A Vivaldi antenna was

$$U(p(k_r(g_r), k_z(g_z)), \theta(g_z), k_z(g_z)) = \begin{cases} U(p(k_r(g_r), k_z(g_z)), \theta(g_\theta), k_z(g_z)) & \text{if } U(p(k_r(g_r), k_z(g)), \theta(g_\theta), k_z(g_z)) \leq 2k_{max} \\ 0 & \text{otherwise} \end{cases} \qquad (25)$$

connected to the vector network analyser (VNA) via a 50 Ω cable. This antenna was manufactured using two layers of Arlon−Diclad 527 with permittivity 2.65 and loss tangent of 0.0022. The antenna was mounted into a waterproof acrylic mounting structure. A polyethylene reservoir was placed under the tank as a safety measure to prevent any accidental oil spills. Owing to the properties of the antenna, which has a support band of 1−6 GHz, an SFCW of 5 GHz with a centre frequency of 3.5 GHz was used in this setup.

The data were reconstructed using a 2.66 GHz PC with Intel i7 processor with 12GB RAM and two Nvidia Tesla C1060 GPUs using Microsoft Visual Studio 7.0 C++ as the development environment. Two versions of the proposed GPGPU algorithm were implemented. The first version used only 1 T device while the second one used both GPU cards. To assess the performance of the proposed technique when executed on a standard Intel Pentium multicore processor, a CPU version of the proposed approach version was implemented using a conventional lookup table (LUT) interpolation approach to emulate the texture memory fetch operation [29]. This technique has a computational complexity of [29]. In both the CPU and GPU approaches, a linear fitting was used since the previous work done by the authors show that it yields high SNR and spatial accurate images [10]. In all the implementations, the NVidia CUFFT library is used to calculate the Fourier transform of the processed datasets. The average transfer time between the host and the device memory for the GPGPU platform was 5.01 ms.

The phantom used in the first three experiments consisted of a polyvinyl chloride (PVC) pipe filled with synthetic foam disks. The PVC pipe has an inner diameter of 10 cm and its length is 90 cm. Aluminium ovoids were used as targets. The length of the ovoids minor and major axis was 1.2 and 3 cm, respectively. The phantom materials present almost no variation in their dielectric permittivity values in the 1−12 GHz frequency range. The final experiment was collected using a phantom whose dielectric properties mimic the average values of human breast tissues. The scan region is formed by glycerin stored inside a styrene-nitril cylinder with a diameter of 13 cm, and the synthetic tumor was formed by a mixture of 85% saline and 15% fructose injected inside a semi-spherical capsule with a diameter of 7 mm. Canola was used as a matching medium. The skin layer was created by covering the container with a 2 mm layer of a mixture formed corn syrup and agar gel described in [30]. To simulate the average dielectric properties of fibroglandular structures, a mixture of 50% wheat flour and 50% saline was used. A melamine coat was used to keep the glycerine from mixing with the fibroglandular tissue mixture. To assess if this coat modified the responses from the wheat−saline mixture, two ovoids with a diameter of 3.5 cm and a height of 4 cm were fabricated and one of them was covered using the waterproof coat. A set of 30 scans was collected using for each ovoid at different locations within the phantom and it was found that the coat did not significantly affect the responses of the simulated fibroglandular tissues. The dielectric permittivity values of the materials used in the support base and the phantoms are shown in Table 1. A photograph of the data acquisition setups can be seen in Fig. 4.

The data collected from four experimental setups were used to determine the feasibility of the proposed approach and assess its spatial accuracy and image quality compared to the Qhull approach. The experimental data acquisition process was performed by rotating the phantom at 5° intervals for a total of 72 positions. In the first three

Table 1 Relative permittivity values of the materials used in the phantom structure and support base

Material	Permittivity value (3 GHz)
PVC	3.2
air	1
maple wood	1.55−1.7
skin	35
agar−corn syrup gel	32
low density breast tissue	9
glycerin	8.9
tumour	55
fructose−saline mixture	53
canola oil	2.5
styrene−acrylonitrile	2.6
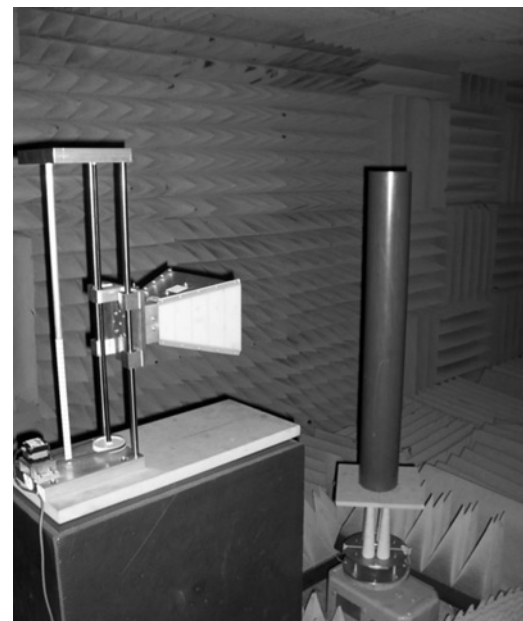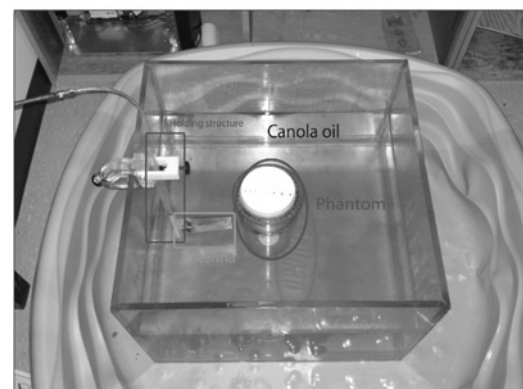
Fig. 4 *Photograph of the data acquisition setup*
a Photograph of the 3D SR data acquisition setup
b Photograph of the BMR data acquisition setup

experiments, the distance between the antenna and the centre of the phantom was set to 70 cm in order to allow the antenna footprint to illuminate the entire phantom and reduce undesirable interferences of antenna early time artefacts. Along the z-axis, the data were acquired using 15 scan planes with a separation of 1 cm. In the fourth

experiment, the distance between the antenna and the centre of the phantom was 20 cm. In this scenario, the early time responses are not as strong as the conductivity of the propagation medium (0.035 S/m) introduces higher losses than the ones present in air.

The performance of the proposed method was quantitatively assessed by calculating the spatial accuracy, SNR and root-mean-square (RMS) error values of the reconstructed images. The spatial accuracy was determined by calculating the difference between the target location and the centroids of their signatures in the reconstructed images. The SNR of the 3D models was calculated as follows

$$\text{SNR} = 20 \cdot \log_{10}\left(\sum_{q=1}^{T} \Gamma_{q,3\text{ dB}}/(T \cdot \sigma^w)\right) \qquad (27)$$

where $\Gamma_{q,3\text{ dB}}$ is the magnitude of the 3 dB point of the qth target signature in the 3D model generated by each algorithm and σ^w is the standard deviation of the background noise. In the following discussion, the centre of the phantom will be denoted as the origin, and the images show the normalised energy of the reconstructed data.

The data collected from four experimental setups were used to determine the feasibility of the proposed approach and assess its spatial accuracy and image quality compared to the Qhull approach, its CPU–LUT counterpart and the current standard technique for cylindrical SR image reconstruction, confocal mapping [5]. In all the experiments, the separation between the targets was at least equal to twice the value of the spatial resolution along the range direction. In the following discussion, the images formed by the single GPU implementation are shown, as no qualitative or SNR and spatial accuracy differences could be found between the two GPU versions of the proposed method.

5 Results and discussion

First, the performance of the proposed approach was evaluated using four groups of 30 simulated datasets. Each group corresponded to one of the four sizes previously mentioned, $127 \times 72 \times 11$, $251 \times 72 \times 11$, $501 \times 150 \times 16$ and $1001 \times 150 \times 16$ points. The datasets were reconstructed using the single and dual GPGPU versions of the proposed approach. Additionally, to compare the performance of the proposed method against the conventional CPU-based interpolation procedures, the data were processed using a CPU version of the proposed method and a wavefront reconstruction approach that used the Qhull approach. The resulting execution times are shown in Table 2. All the execution times reported in this work include the transfer time between the GPU and the CPU. Note how the execution time of the GPGPU technique is at least two orders of magnitude faster than the Qhull interpolation

method. The speed improvement compared with the CPU implementation is about 28 times. Additionally, note how the speed increases when the two GPU devices are used in around 2.05 times. This is because that each plane can be processed independently of the others in each of the two interpolation processes; thus dividing the computational load between the two graphic devices further reducing the time required to reconstruct a 3D image. Additionally, the SNR and spatial accuracy differences between the proposed technique were compared and the Qhull approach was calculated and tested for statistical significance using the Student's t-test. No significant differences ($P < 0.05$) were found in the images formed from the simulations. Additionally, no significant differences ($P < 0.05$) could be found between the SNR and spatial accuracy values of the images formed from simulated datasets using the single and dual GPU implementations of the proposed method.
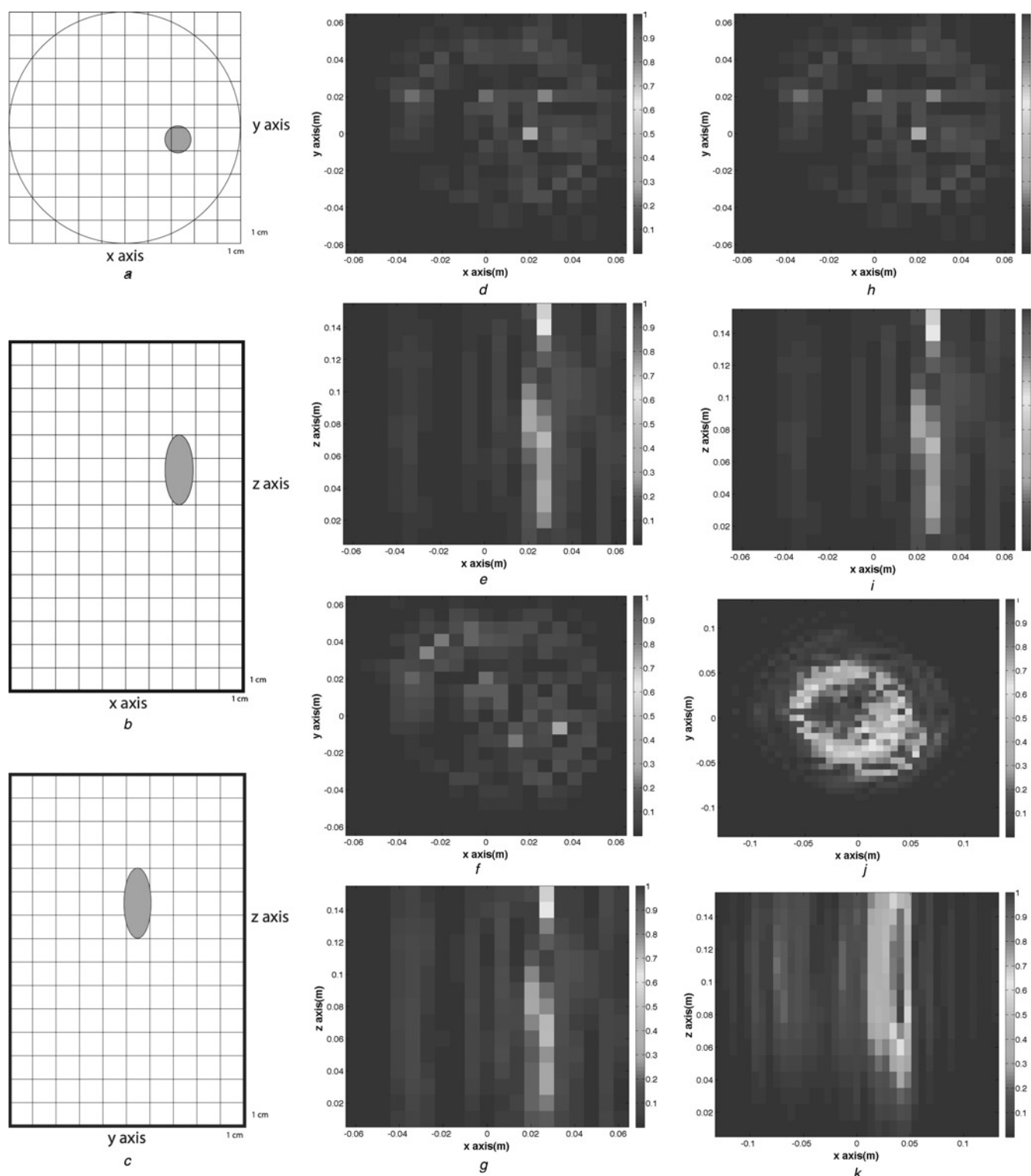
Next, the experimental feasibility of the proposed method was assessed using four experimental datasets. The setup in experiment 1 only contained one target was present and it is shown in Figs. 5a–c. To make it easier to visualise the performance of the proposed method, the axial and coronal cross-sections of each reconstructed target are displayed. To better assess the location and dimensions of the target signatures, the phantom surface was removed using the method proposed by the authors in [31]. The axial and coronal images of the target signature generated by the proposed method are shown in Figs. 5d and e. The results yielded by the Qhull approach can be seen in Figs. 5f and g. The axial and coronal cross-sections obtained using the CPU version of the proposed method are illustrated in Figs. 5h and i. Finally, the axial and coronal images generated using the confocal mapping approach are shown in Figs. 5j and k. The SNR of the image formed using the proposed approach in this experiment was 8.81 dB, which is slightly larger than the values obtained for the images formed using the Qhull, CPU–LUT and confocal mapping approaches (8.77, 8.8 and 2.94 dB, respectively).

The setup used in experiment 2 is shown in Figs. 6a–c. The axial and coronal images generated by the proposed approach are shown in Figs. 6d and e. The resulting cross-sections of the target responses formed by the Qhull approach and CPU–LUT approaches are shown in Figs. 6f and g and Figs. 6h and i, respectively. Finally, the axial and coronal views of the target responses obtained from processing the dataset using the confocal mapping algorithm are shown in Figs. 6j–l. Note how in all the reconstructed images the locations of the reconstructed target signatures are consistent with their locations on the experimental setup. The image reconstructed using the proposed method had an SNR of 8.5 dB. The SNR of the images produced using the Qhull and the CPU–LUT approach were 8.48 dB for both. The SNR for the 3D image generated using the confocal mapping algorithm was 3.36 dB.

Table 2 Execution times of the 3D wavefront reconstruction approach for cylindrical scan geometries using the Qhull approach and the CPU, single-GPU and multi-GPU versions of the proposed approach

| Technique/size	$127 \times 72 \times 11$	$251 \times 72 \times 11$	$501 \times 150 \times 16$	$1001 \times 150 \times 16$
Qhull	7.81	27.5	465.47	1004.67
proposed method CPU	1.65	3.85	39.56	190.8
proposed method single GPU	0.034	0.124	1.52	4.34
proposed method dual GPU	0.016	0.060	0.74	2.11

All times are in seconds

Fig. 5 *Experimental feasibility of the proposed method was assessed using four experimental datasets in experiment one*

a Axial view of the phantom setup in experiment one
b Coronal view of the phantom setup in experiment one
c Sagital view of the phantom setup in experiment one
d Axial view of the reconstructed target signature using the proposed method
e Coronal view of the reconstructed target signature using the proposed method
f Axial view of the reconstructed target signature using the Qhull approach
g Coronal view of the reconstructed target signature using the Qhull approach
h Axial view of the reconstructed target signature using the CPU–LUT approach
i Coronal view of the reconstructed target signature using the CPU–LUT approach
j Axial view of the reconstructed target signature using the confocal-mapping approach
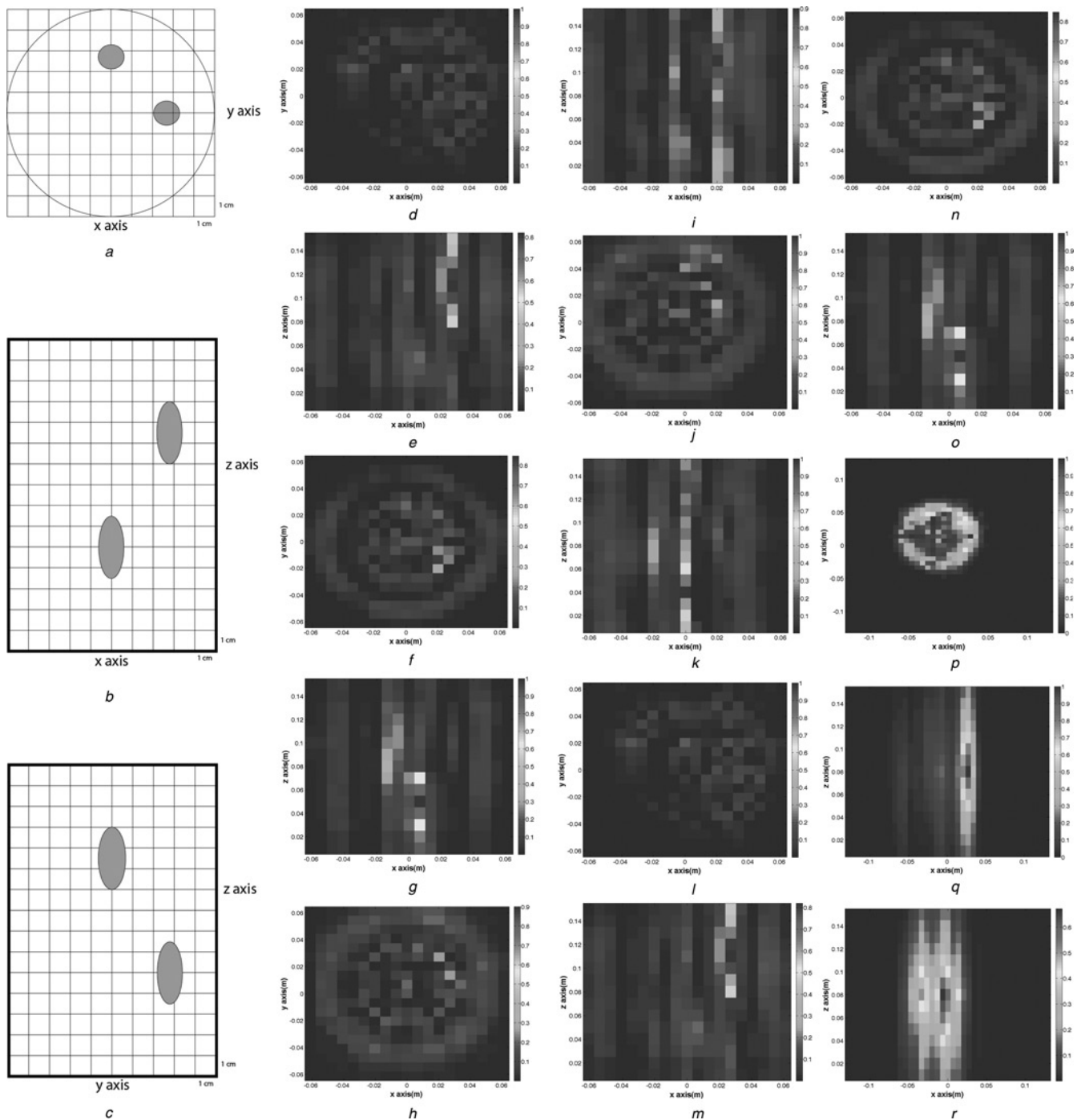*k* Coronal view of the reconstructed target signature using the confocal-mapping approach
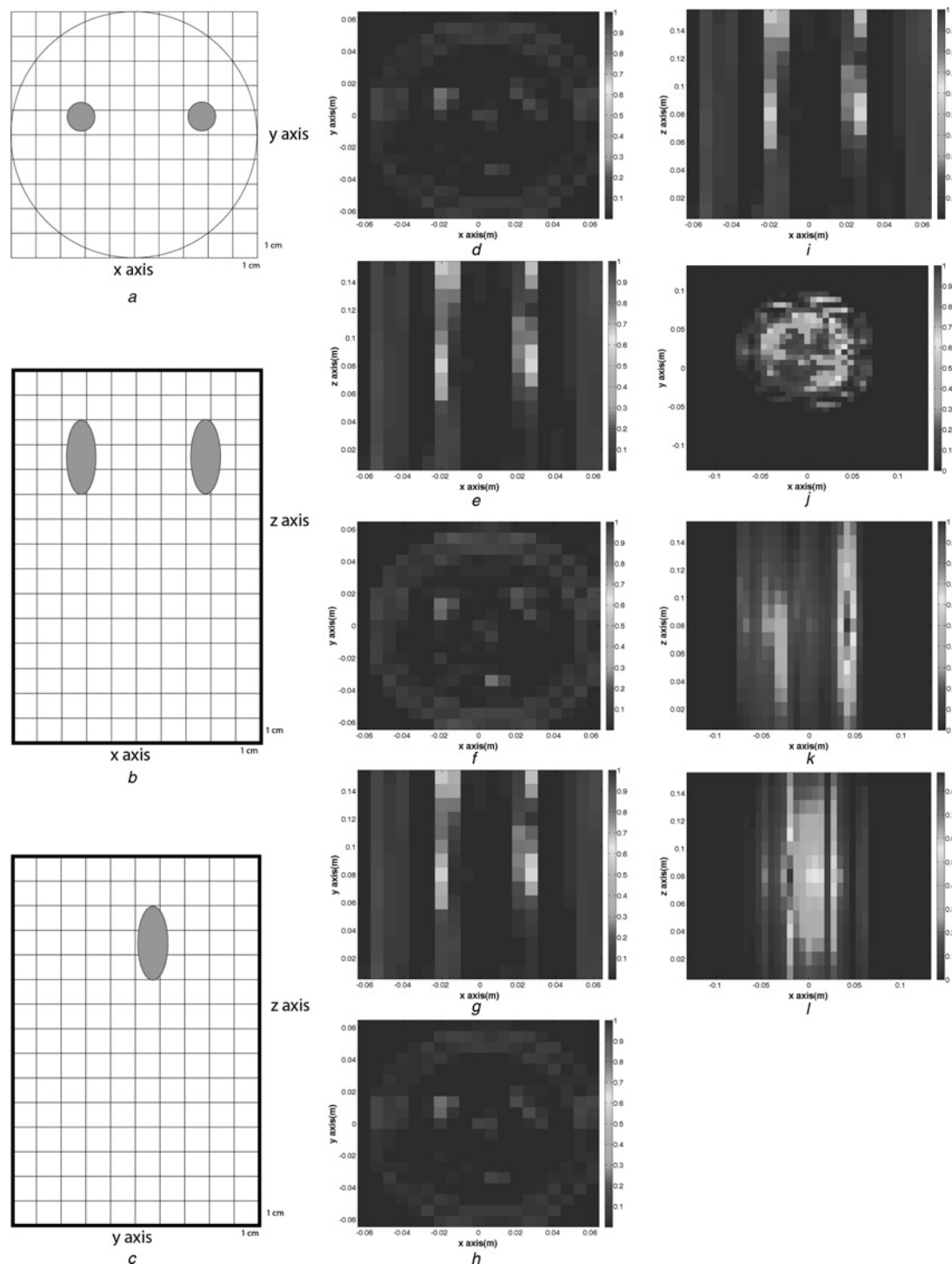
Fig. 6 *Experimental feasibility of the proposed method was assessed using four experimental datasets in experiment two*

a Axial view of the phantom setup in experiment two
b Coronal view of the phantom setup in experiment two
c Sagital view of the phantom setup in experiment two
d Axial view of the reconstructed target signatures using the proposed method
e Coronal view of the reconstructed target signatures using the proposed method
f Axial view of the reconstructed target signatures using the Qhull approach
g Coronal view of the reconstructed target signatures using the Qhull approach
h Axial view of the reconstructed target signatures using the CPU–LUT approach
i Coronal view of the reconstructed target signatures using the CPU–LUT approach
j Axial view of the reconstructed target signatures using the confocal mapping approach
k Coronal view of the first reconstructed target signatures using the confocal mapping approach
l Coronal view of the second reconstructed target signatures using the confocal mapping approach

The setup used in experiment 3 is displayed in Figs. 7*a*–*c*. The results of the proposed approach and are shown in Figs. 7*d*–*g*. The SNR of the image yielded by the proposed method was 6.72 dB. The axial and coronal target images produced by the Qhull approach are shown in Figs. 7*h*–*k*. The results of the CPU–LUT and confocal mapping

Fig. 7 *Experimental feasibility of the proposed method was assessed using four experimental datasets in experiment three*

a Axial view of the phantom setup in experiment three
b Coronal view of the phantom setup in experiment three
c Sagital view of the phantom setup in experiment three
d Axial view of the reconstructed first target signature using the proposed method
e Coronal view of the reconstructed first target signature using the proposed method
f Axial view of the reconstructed second target signature using the proposed method
g Coronal view of the reconstructed second target signature using the proposed method
h Axial view of the reconstructed first target signature using the Qhull approach
i Coronal view of the reconstructed first target signature using the Qhull approach
j Axial view of the reconstructed second target signature using the Qhull approach
k Coronal view of the reconstructed second target signature using the Qhull approach
l Axial view of the reconstructed first target signature using the CPU–LUT approach
m Coronal view of the reconstructed first target signature using the CPU–LUT approach
n Axial view of the reconstructed second target signature using the CPU–LUT approach
o Coronal view of the reconstructed second target signature using the CPU–LUT approach
p Axial view of the reconstructed target signatures using the confocal mapping approach
q Coronal view of the reconstructed first target signature using the confocal mapping approach
r Coronal view of the reconstructed second target signature using the confocal mapping approach

approaches are shown in Figs. 7*l*−*o* and Figs. 7*p*−*r*, respectively. The SNR of the 3D models generated by the Qhull, CPU−LUT, and confocal mapping methods were 6.45, 6.7 and 2.93 dB, respectively.

The experimental setup in experiment 4 is shown in Figs. 8*a* and *b*. The image produced by the proposed approach is shown in Fig. 8*c*. The results of using the Qhull approach and the CPU version of the proposed approach are shown in Figs. 8*d* and *e*. The SNR values of these images are 5.58 and 5.57 dB, respectively. The image generated by the confocal mapping approach is shown in Fig. 8*f*. This image has an SNR of 2.13 dB. The SNR values from the images formed using the confocal mapping approach are consistent with the values reported in previous studies [9]. Additionally, note how there are no high magnitude artefacts in the images formed using a wavefront reconstruction-based approach. The locations and position error of the target signatures in each experiment are shown in Table 3. The SNR values are summarised in Table 4. The RMS error between the proposed method, the Qhull

Table 4 SNR values in each experiment

Experiment	Qhull, dB	Proposed method, dB	CPU−LUT, dB	Confocal mapping, dB
1	8.77	8.81	8.8	2.94
2	8.48	8.5	8.48	3.36
3	6.45	6.72	6.7	2.93
4	5.58	5.57	5.57	2.13

Table 5 RMS difference values in each experiment

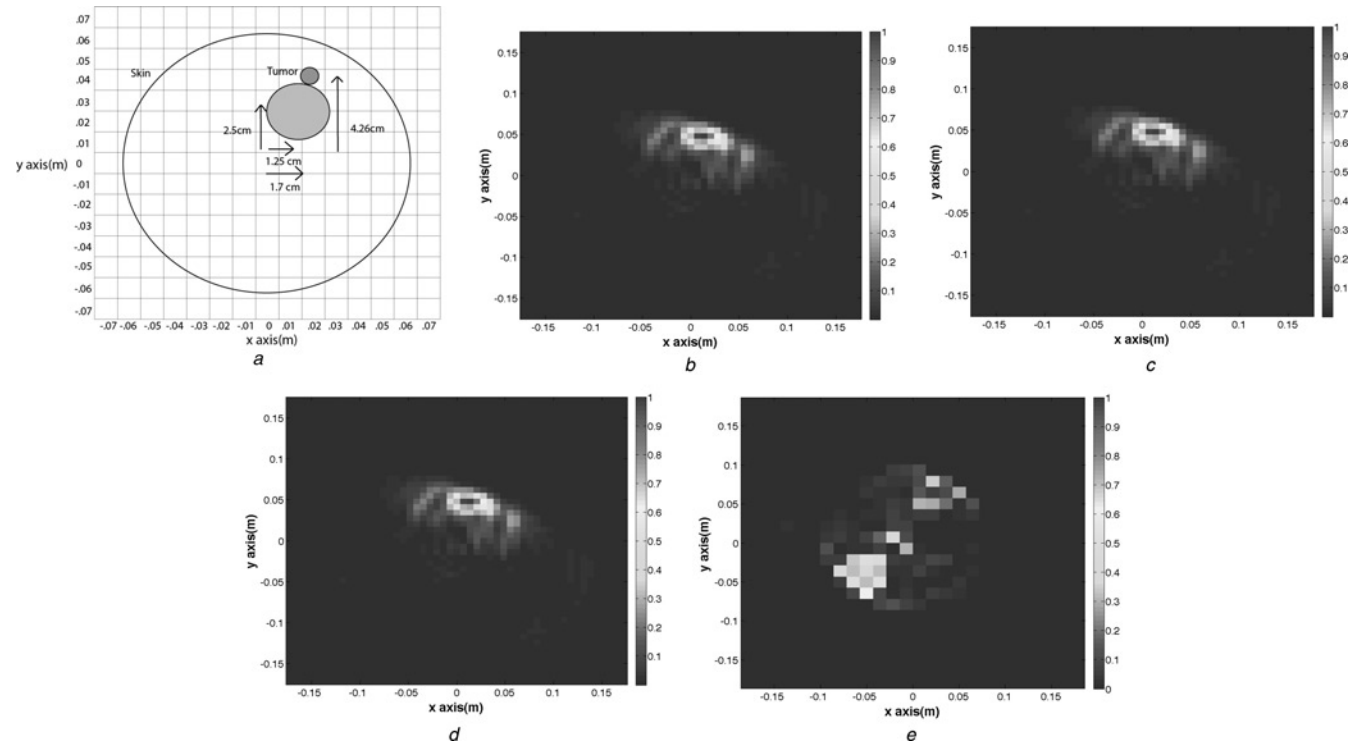| Experiment	Qhull	Confocal mapping
1	2.5×10^4	2×10^3
2	7.85×10^5	2.2×10^3
3	1.14×10^4	2.8×10^3
4	1.72×10^6	2.7×10^3

Fig. 8 *Experimental feasibility of the proposed method was assessed using four experimental datasets in experiment four*

a Axial view of the phantom setup in experiment four
b Reconstructed model from the data collected in experiment four using the proposed method
c Reconstructed model from the data collected in experiment four using the Qhull approach
d Reconstructed model from the data collected in experiment four using the CPU−LUT version of the proposed method
e Reconstructed model from the data collected in experiment four using the confocal mapping approach

Table 3 Spatial error values obtained in each experiment

Target	Target location, cm	Qhull error, mm	Proposed method error, mm	CPU−LUT error, mm	Confocal mapping error, mm
1a	−0.5, 2.2, 10	1.8, 2, 0.5	1.8, 2, 0.5	1.8, 2, 0.5	−0.1, 28, 20
2a	2.6, 0.63, 12	1.2, 0.3, 0	1.2, 0.3, 0	1.2, 0.3, 0	23, 16, −40
2b	−2.1, 0.63, 12	1, 0.3, 0	1, 0.3, 0	1, 0.3, 0	0.1, 50, −40
3a	2.6, 0, 11	1.2, 0, 0	1.2, 0, 0	1.2, 0, 0	0, 14. −30
3b	0, 2.6, 5.5	0, 1.2, 5	0, 1.2, 5	0, 1.2, 5	0.5, 2.4, 25
4a	4.26, 1.7	5, 0.2	5, 2	5, 2	13, 3

Table 6 Execution times in each experiment

Experiment	Single GPU	Dual GPU	CPU–LUT	Qhull	Confocal mapping
1	0.69	0.33	16.7	309.21	3.2
2	0.70	0.34	17.5	310.45	3.35
3	0.70	0.34	17.3	310.71	3.15
4	0.046	0.024	1.3	20.6	0.18

All times are in seconds

approach and the confocal mapping algorithm are displayed in Table 5. The execution times for each dataset using the proposed method, its CPU counterpart and the Qhull approach are illustrated in Table 6.

6 Conclusions

In this paper, a real-time 3D reconstruction approach for radar datasets recorded in near-field cylindrical scan geometries was proposed. The proposed algorithm is based on a novel interpolation technique that does not require a triangulation procedure, reducing its computational complexity. Since the proposed technique is easily parallelisable, it was implemented on a GPGPU platform in order to take advantage of the arithmetic capabilities and memory bandwidth of these devices. The performance of the proposed method was assessed using experimental data sets collected from phantoms that mimic cylindrical radar imaging scenarios with high and moderate dielectric contrast between the propagation media and the targets.

Compared with the results obtained using the Qhull approach, the images generated by the proposed technique using experimental datasets had a similar spatial accuracy, slightly better SNR values and a reduced execution time. The proposed method generates images with noticeable improvements in SNR and spatial accuracy. Furthermore, the proposed method did not introduce any discernible artefacts in the reconstructed datasets. The acceleration provided by the GPGPU platform solved one of the most important shortcomings of wavefront reconstruction approaches when compared to confocal mapping methods, which was their longer execution time.

The proposed approach is capable of generating 3D images in real-time for datasets with dimensions similar to the ones used in BMRI and MWI scenarios. When executed on a single GPU, the proposed approach achieved a speed improvement of 160 times compared to conventional interpolation techniques for non-evenly sampled spaces, and 28 times compared with its CPU-based counterpart. Additionally, a second implementation of the proposed algorithm that uses two GPGPU devices yielded a speed improvement of 2.05 times compared to the single GPGPU version, suggesting the potential of multi-GPGPU platforms.

7 Acknowledgment

8 References

1 Bryant, M.L., Gostin, L.L., Soumekh, M.: '3-D E-CSAR imaging of a T-72 tank and synthesis of its SAR reconstructions', *IEEE Trans. Aerosp. Electron. Syst.*, 2003, **39**, (1), pp. 211–227

2 Burki, J., Barnes, C.F.: 'Slant plane CSAR processing using householder transform', *IEEE Trans. Image Process.*, 2008, **17**, (10), pp. 1900–1907

3 Lin, Y., Hong, W., Tan, W., Wu, Y.: 'Extension of range migration algorithm to squint circular SAR imaging', *IEEE Geosci. Remote Sens. Lett.*, 2011, **8**, (99), pp. 651–655

4 Ertin, E., Moses, R.L., Potter, L.C.: 'Interferometric methods for three-dimensional target reconstruction with multipass circular SAR', *IET Radar Sonar Navig.*, 2010, **4**, (3), pp. 464–473

5 Fear, E.C., Stuchly, M.A.: 'Microwave detection of breast cancer', *IEEE Trans. Microw. Theory Tech.*, 2000, **48**, (11), pp. 1854–1863

6 Kaestner, A.P., Baath, L.B.: 'Microwave polarimetry tomography of wood', *IEEE Sens. J.*, 2005, **5**, (2), pp. 209–215

7 Flores-Tapia, D., Thomas, G., Pistorius, S.: 'A wavefront reconstruction method for 3D cylindrical subsurface radar imaging', *IEEE Trans. Image Process.*, 2008, **17**, (10), pp. 1908–1925

8 Bond, E.J., Xu, Li, Hagness, S.C., Van Veen, B.D.: 'Microwave imaging via space-time beamforming for early detection of breast cancer', *IEEE Trans. Antennas Propag.*, 2003, **51**, (8), pp. 1690–1705

9 Klemm, M., Craddock, I.J., Leendertz, J.A., Preece, A., Benjamin, R.: 'Radar-based breast cancer detection using a hemispherical antenna array—experimental results', *IEEE Trans. Antennas Propag.*, 2009, **57**, (6), pp. 1692–1704

10 Flores-Tapia, D., Thomas, G., Pistorius, S.: 'A comparison of interpolation methods for breast microwave radar imaging'. Proc. 2009 Annual Int. Conf. IEEE Engineering in Medicine and Biology Society, Minneapolis, MN, USA, September 2009, pp. 2735–2738

11 'Mammography and beyond: developing techniques for the early detection of breast cancer' (Inst. Med., Nat. Academy Press, Washington, DC, 2000)

12 Flores-Tapia, D., Pistorius, S.: 'A real time breast microwave radar imaging reconstruction technique using SIMT based interpolation'. Proc. 2010 17th IEEE Int. Conf. on Image Processing, Hong Kong, September 2010, pp. 1389–1392

13 Pratx, G., Chinn, G., Olcott, P.D., Levin, C.S.: 'Fast, accurate and shift-varying line projections for iterative reconstruction using the GPU', *IEEE Trans. Med. Imaging*, 2009, **28**, (3), pp. 435–445

14 Fang, Xu, Mueller, K.: 'Accelerating popular tomographic reconstruction algorithms on commodity PC graphics hardware', *IEEE Trans. Nucl. Sci.*, 2005, **52**, (3), pp. 654–663

15 Taylor, Z.A., Cheng, M., Ourselin, S.: 'High-speed nonlinear finite element analysis for surgical simulation using graphics processing units', *IEEE Trans. Med. Imaging*, 2008, **27**, (5), pp. 650–663

16 Friedrichs, M.S., Eastman, P., Vaidyanathan, V., *et al.*: 'Accelerating molecular dynamic simulation on graphics processing units', *J. Comput. Chem.*, 2009, **30**, (6), pp. 864–872

17 Owens, J.D., Houston, M., Luebke, D., Green, S., Stone, J.E., Phillips, J.C.: 'GPU computing', *Proc. IEEE*, 2008, **96**, (5), pp. 879–899

18 Soumekh, M.: 'Synthetic aperture radar signal processing with MATLAB algorithms' (Wiley-Interscience, New York City, New York, USA, 1999)

19 Barber, C.B., Dobkin, D.P., Huhdanpaa, H.: 'The quickhull algorithm for convex hulls', *ACM Trans. Math. Softw.*, 1996, **22**, (4), pp. 469–483

20 Späth, H.: 'Two dimensional spline interpolation algorithms' (A. K. Peters Ltd., Wellesley, MA, USA, 1995)

21 Sorensen, T., Schaeffter, T., Noe, K., Hansen, M.: 'Accelerating the nonequispaced fast Fourier transform on commodity graphics hardware', *IEEE Trans. Med. Imaging*, 2008, **27**, (4), pp. 538–547

22 Sorensen, T., Atkinson, D., Schaeffter, T., Hansen, M.: 'Real-time reconstruction of sensitivity encoded radial magnetic resonance imaging using a graphics processing unit', *IEEE Trans. Med. Imaging*, 2009, **28**, (12), pp. 1974–1985

23 Stone, S., Haldar, J., Tsao, S., Hwu, W.W., Sutton, B., Liang, Z.-P.: 'Accelerating advanced MRI reconstructions on GPUs', *J. Parallel Distrib. Comput.*, 2008, **68**, (10), pp. 1307–1318

24 Beatty, P.J., Nishimura, D.G., Pauly, J.M.: 'Rapid gridding reconstruction with a minimal oversampling ratio', *IEEE Trans. Med. Imaging*, 2005, **24**, (6), pp. 799–808

25 Bronstein, M.M., Bronstein, A.M., Zibulevsky, M., Azhari, H.: 'Reconstruction in diffraction ultrasound tomography using nonuniform FFT', *IEEE Trans. Med. Imaging*, 2002, **21**, (11), pp. 1395–1401

26 Sok-Son, J., Thomas, G., Flores, B.C.: 'Range-doppler radar imaging and motion compensation' (Artech House, Inc., Norwood, MA, USA, 2001)

27 NVidia Corporation Inc.: 'CUDA C programming guide' (San Jose, 2010)

28 Flores-Tapia, D., Thomas, G., Sabouni, A., Noghanian, S., Pistorius, S.: 'Breast tumor microwave simulator based on a radar signal model'. IEEE Int. Symp. on Signal Processing and Information Technology, Vancouver, BC, Canada, August 2006, pp. 1–6

29 Sharma, G.: 'Digital color imaging handbook' (CRC Press, Boca Raton, FL, USA, 2002)

30 Li, D., Meaney, P.M., Paulsen, K.D.: 'Conformal microwave imaging for breast cancer detection', *IEEE Trans. Microw. Theory Tech.*, 2003, **51**, (4), pp. 1179–1185

31 Flores-Tapia, D., Thomas, G., Pistorius, S.: 'Skin surface removal on breast microwave imagery'. Proc. SPIE Medical Imaging 2006 Conf., San Diego, CA, USA, January 2006, pp. 61433A.1–61433A.9